

Testing Accretion Disk Structure with Suzaku data of LMC X-3

Aya Kubota¹, Chris Done², Shane W. Davis³, Tadayasu Dotani⁴, Tsunefumi Mizuno⁵ and Yoshihiro Ueda⁶
 aya@shibaura-it.ac.jp

ABSTRACT

The Suzaku observation of LMC X-3 gives the best data to date on the shape of the accretion disk spectrum. This is due to the combination of very low absorbing column density along this line of sight which allows the shape of the disk emission to be constrained at low energies by the CCD's, while the tail can be simultaneously determined up to 30 keV by the high energy detectors. These data clearly demonstrate that the observed disk spectrum is broader than a simple 'sum of blackbodies', and relativistic smearing of the emission is strongly required. However, the intrinsic emission should be more complex than a (color-corrected) sum of blackbodies as it should also contain photo-electric absorption edges from the partially ionised disk photosphere. These are broadened by the relativistic smearing, but the models predict ~ 3 –5 per cent deviations for 1/3–1 solar abundance around the edge energies, significantly stronger than observed. This indicates that the models need to include more physical processes such as self-irradiation, bound-bound (line) absorption, and/or emission from recombination continua and/or lines. Alternatively, if none of these match the data, it may instead require that the accretion disk density and/or emissivity profile with height is different to that assumed. Thus these data demonstrate the feasibility of observational tests of our fundamental understanding of the vertical structure of accretion disks.

Subject headings: accretion, accretion disks—black hole physics—stars:individual (LMC X-3)—X-rays:stars

1. Introduction

It is important to study the emission from the accretion disk to understand how the gravita-

tional energy is converted to radiation. The simplest models of accretion disk spectra assume that the gravitational energy dissipated at each radius thermalizes to a blackbody spectrum. Summing it over all radii, under an appropriate inner boundary condition, produces the well-known Shakura & Sunyaev (1973) disk model. This is derived in Newtonian gravity, but was extended to full general relativity by Novikov & Thorne (1973). The maximum temperature produced by a disk accreting close to the Eddington limit around a $10 M_{\odot}$ black hole is 1–2 keV, easily observable with X-ray satellites, whereas a similarly Eddington limited Active Galactic Nuclei (AGN) of $10^7 M_{\odot}$ has a temperature of 30–60 eV, in the unobservable EUV regime. Thus stellar remnant black hole binary (hereafter BHB) systems give a much better test of disk models than AGN.

¹Department of Electronic Information Systems, Shibaura Institute of Technology, 307 Fukasaku, Minumaku, Saitama-shi, Saitama 337-8570, Japan

²Department of Physics, University of Durham, South Road, Durham, DH1 3LE, UK

³School of Natural Sciences, Institute for Advanced Study, Einstein Drive, Princeton, NJ 08540, USA, Chandra Fellow

⁴Institute of Space and Astronautical Science, Japan Aerospace Exploration Agency, 3-1-1 Yoshinodai, Sagamihara, Kanagawa 229-8510, Japan

⁵Department of Physics, Hiroshima University, 1-3-1 Kagamiyama, Higashi-Hiroshima, Hiroshima 739-8526, Japan

⁶Department of Astronomy, Kyoto University, Sakyo-ku, Kyoto 606-8502, Japan

The emission from each radius is a true blackbody only when the disk is effectively optically thick to absorption at all frequencies. Free-free (continuum) absorption drops as the frequency increases, so the highest energy photons from each radii are unlikely to thermalize. This forms instead a modified (or diluted) blackbody, with effective temperature higher than that for complete thermalization by a factor of f_{col} (termed a color temperature correction). The full disk spectrum is then a sum of these modified blackbodies, but this can likewise be approximately described by a single color temperature correction to a sum of blackbody disk spectrum (Shimura & Takahara 1995). However, continuum processes do not necessarily dominate the total absorption at all frequencies. Bound-free (photo-electric) absorption from partially ionised metals can be important, especially at high frequencies where the free-free absorption becomes less significant (Davis et al. 2005). This imprints atomic features onto the emission from each radius, distorting the spectrum from a smooth continuum. The strength of these features is set by radiative transfer through the vertical structure of the photosphere, so they are one of the few diagnostics of the internal disk properties (Done & Davis 2008).

Thus the intrinsic spectrum from each radius can be complex, but each of these is smeared out by the combination of special and general relativistic effects which arise from the rapid rotation of the emitting material in a strong gravitational field (Cunningham 1975). The resultant smeared spectra are summed together to form the total disk emission, which is not that different from a sum of smeared color temperature corrected blackbody spectra (Davis et al. 2005; Davis & Hubeny 2006; Done & Davis 2008). We need excellent data in order to detect these smeared spectral features, and use them to test our understanding of the disk vertical structure.

The BHB LMC X-3 is the best object currently known for this. It has the lowest absorption column density of any BHB which shows disk dominated spectra, extending the bandpass over which the data can constrain the models down to the softest X-ray energies. Additionally, the system parameters are fairly well determined, especially distance which is known to better than 10 per cent due to its location in the Large Magellanic Cloud.

Thus the conversion of flux to luminosity is subject to smaller uncertainties than for any other BHB. This combination of properties means LMC X-3 offers a unique laboratory for testing our understanding of accretion disk physics.

Here we use data from a Suzaku (Mitsuda et al. 2007) observation of the disk dominated state in this object. This satellite combines moderate spectral resolution CCD's useful to constrain 0.7-10 keV spectrum of the source, together with the Si PIN photo-diodes of the non-imaging Hard X-ray Detector (HXD, Takahashi et al. 2007) which can simultaneously determines the 12-30 keV spectrum. Thus these data give a complete picture of the emission, being able to constrain the (weak) tail to higher energies which otherwise gives a significant source of uncertainty in reconstructing the disk spectrum from CCD data alone.

The spectrum of LMC X-3 during this observation is dominated by a clear disk component with luminosity around 10 per cent of the Eddington limit. This is low enough to avoid the multiple uncertainties which arise at higher luminosities, where the disk may puff up due to radiation pressure, advection of radiation may become important, and strong winds from the inner disk can distort the spectrum both through absorption and from changing the intrinsic disk spectrum due to the mass loss. Thus these observations give the most sensitive test to date of our understanding of a 'clean' accretion disk to compare with the models.

2. Observation and Data reduction

We observed LMC X-3 with Suzaku from 2008 December 22 UT07:14 through December 23 UT20:49 (epoch 5). Suzaku carries 4 X-ray telescopes (XRT, Serlemitsos et al. 2007), each with a focal-plane X-ray CCD camera (X-ray Imaging Spectrometer; XIS, Koyama et al. 2007) operating in the energy range of 0.2–12 keV. Three of the XIS (XIS0, 2, 3) have front-illuminated (FI) CCDs, while XIS1 utilizes a back-illuminated (BI) CCD, achieving an improved soft X-ray response but poorer hard X-ray sensitivity. Since XIS2 is no longer available, we use the two remaining FI-CCDs (XIS03) together with the BI-CCD (XIS1). We combine these with data from the Si PIN photo-diodes of the HXD (Takahashi et al. 2007),

which covers the 10–70 keV energy band.

The source was centered in the XIS field of view. The XIS were operated with the 1/4 window option so that pileup did not become significant. We use version 2.2.11.22 of the pipeline provided by the Suzaku team, and the XIS data are screened using the standard criteria (i.e. only GRADE0, 2, 3, 4, 6 events are accumulated, time interval after passage through the South Atlantic Anomaly is larger than 436 seconds, the object is at least 5° and 20° above the rim of the Earth during night and day, respectively). This gives a net exposure of 73.98 ks.

We extract XIS events from both 5×5 and 3×3 editmodes using a circular region with a radius of $4'.3$ centered on the image peak. This is larger than the window size so the effective extraction region is the intersection of the rectangular window with this circle. We use FTOOL XISRMFGN (VERSION 2007-05-14) and XISSIMARFGN (VERSION 2009-01-08) to calculate the response matrix and auxiliary response of the instrument. We co-add the data from the two FI CCDs as these are very similar, and generate the co-added response for this XIS03 spectrum using the FTOOLS ADDRMF and ADDARF. We add systematic errors of 1% to each energy bin for both XIS03 and XIS1 spectra.

The source is bright, with count rate from XIS1 of 24 cts s^{-1} in the range of 0.7–10 keV, which corresponds to $3.1 \times 10^{-10} \text{ erg s}^{-1} \text{ cm}^{-2}$. Though background can be important towards the highest energy end of this bandpass, the large point spread function of Suzaku means that the 1/4 window data cannot be used to simultaneously determine the background as there is no source-free region. Instead we use the Lockman hole data obtained by Suzaku from 2009 June 12 UT 07:17 through June 14 UT01:31 with an exposure of a net exposure of 92 ks, using the same shaped (intersection of circle and rectangle) region. The background levels are negligible in soft energy band, and reach to $\sim 0.7\%$ and $\sim 5\%$ of our LMC X-3 data at 8 keV, for XIS03 and XIS1, respectively. In this paper, we used the 0.7–10 keV band and the 0.7–8 keV band for XIS03 and XIS1, respectively. We show the background subtracted XIS03 and XIS1 spectra in Fig. 1.

The HXD was operated in the nominal mode throughout the observations. We use the standard pipeline processed PIN data (object is at least

5° above the earth rim, time interval after passage through the South Atlantic Anomaly is longer than 500 seconds, and cutoff rigidity is greater than 6 GV). We extract background from the same goodtime intervals of the PIN background model based on LCFITDT method (2.0VER0804) provided by the HXD team for each observation (Fukazawa et al. 2009). Here we note that the HXD-PIN background model is aimed to reproduce the non X-ray background. The source exposure is corrected for the 7.3 % deadtime, which is calculated from the pseudo event rates (Takahashi et al. 2007; Kokubun et al. 2007) by using the FTOOL HXDDTCOR, giving a net exposure of 70.03 ks. This is $\sim 25\%$ less than the XIS, but the source shows little variability so we do not exclude any XIS data in order to have only exactly simultaneous data. These data show that the source is not significantly detected at the highest energies, so we restrict the fit range to 12–30 keV using the appropriate response AE_HXD_PINXINOME5_20080716.RSP.

The background subtracted PIN spectrum is shown in Fig. 1 together with the XIS spectra. This has a 12–30 keV count rate of 0.076 cts s^{-1} . This corresponds to a flux of $2.2 \times 10^{-11} \text{ erg s}^{-1} \text{ cm}^{-2}$, which is only ~ 4 times higher than flux of the cosmic X-ray background (CXB) in the same energy range. Thus the CXB is not negligible, and we include this as a fixed exponentially cutoff PL (Boldt 1987) in all our spectral modeling for the PIN data¹.

¹http://heasarc.gsfc.nasa.gov/docs/suzaku/analysis/pin_cxb.html

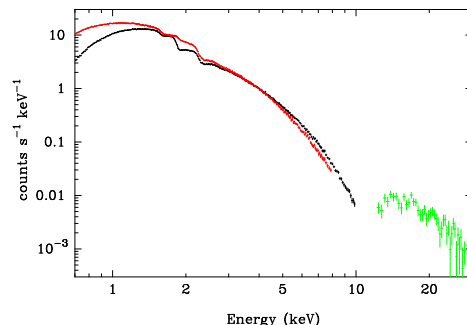


Fig. 1.— The background subtracted X-ray spectra of LMC X-3 obtained with XIS03 (black), XIS1(red) and the HXD PIN(green).

3. Analyses and Results

We describe here the system parameters of LMC X-3 adopted in this paper. LMC X-3 is a persistent source, so the emission from the outer accretion disk always contributes to the optical spectrum, and X-ray irradiation can alter the structure and spectrum of the companion star. This introduces some uncertainty in determining the properties of the companion, and hence the mass of the black hole (van der Klis et al. 1985; Cowley et al. 1983; Soria et al. 2001; Negueruela & Coe 2002). Taking account the uncertainties, we consider the black hole mass in the range of $7\text{--}9M_{\odot}$ and inclinations of $50^{\circ}\text{--}67^{\circ}$. Thus for each physical model (KERRBB and BHSPec² in XSPEC) we report fit values over this range, showing also results for the specific combination of $7M_{\odot}$ and inclination of 67° used by Davis et al. (2006). We assume a source distance of 52 kpc (di Benedetto 1997).

We use the XSPEC spectral fitting package. Large fit residuals due to calibration uncertainties are often observed near the edge structures of the XIS/XRT instrumental responses. We exclude energy range of 1.6–2.0 keV and 2.2–2.4 keV, and model the remaining instrumental feature at ~ 3.2 keV by gold M edge by a gaussian line with fixed gaussian width of 0.1 keV as is done in Kubota et al. (2007).

The absorption column density is well determined as $3.8 \times 10^{20} \text{ cm}^{-2}$ (Page et al. 2003) from the depths of edges measured by the XMM-Newton Reflection Grating Spectrometer data. This is consistent with most of the absorption being due to our own Galaxy as the column density along this line of sight is $3.2 \times 10^{20} \text{ cm}^{-2}$ as measured by radio observations (Nowak et al. 2001). However, low-energy calibration (especially the quantum efficiency) of the Suzaku XIS suffers from relatively large systematic errors due to the uncertainties of the contamination thickness and its composition. To minimize the impact of these systematic errors while keeping good low-energy coverage, we restricted the energy range above 0.7 keV in the spectral analysis. In this energy range with the calibration data base (CALDB: VERSION XIS20090203), we estimate the system-

atic error in determining N_{H} is about a few times 10^{20} cm^{-2} (XIS team, private communication). Because this is comparable to the column density to LMC X-3, we allow N_{H} (described using PHABS) to be free in the spectral analysis unless otherwise stated.

When we analyze the disk emission, it is important to model the power-law component appropriately, because its low-energy part sometimes affect the fitting of the disk emission. A simple power law (hereafter PL) plus CXB fit to the PIN data alone in the 12–30 keV band gives a photon spectral index of 1.66–2.38 with the best fit value of 2.01. Because the power-law component in the high/soft state usually has a photon index larger than 2.0 (e.g., Done et al. 2007 and references therein), we consider that the true index of LMC X-3 lies between 2.00–2.38. Therefore, we constrain the index in this range in the spectral analysis rather than allowing it to be free. Otherwise, the power-law component would be optimized to fill the fit residuals in the low-energy band, where the statistics are much better than those of the HXD PIN, and the best-fit power-law index could significantly deviate from the true slope in the hard energy band.

3.1. Empirical modeling of the disk: DISKBB

In order to compare the spectral data with the previous observations, we first use the common black hole spectral model of an absorbed disk plus power law. The simplest disk model is DISKBB, which has a temperature distribution $T(r) \propto r^{-3/4}$, i.e. has no stress free inner boundary condition (Mitsuda et al. 1984; Makishima et al. 1986).

Figure 2 shows the XIS and the HXD/PIN spectra with this best fit DISKBB plus PL model, with parameters given in table 1. The spectrum is well fit ($\chi^2/dof = 770.25/706$) by the dominant DISKBB component with T_{in} of 0.84 keV. The 0.7–30 keV flux is estimated as $3.30 \times 10^{-10} \text{ erg s}^{-1} \text{ cm}^{-2}$, which gives an absorbed X-ray luminosity as $1.07 \times 10^{38} \text{ erg s}^{-1}$ for an isotropic emission at $D = 52$ kpc. This luminosity is about 10% of the Eddington luminosity for a $7 M_{\odot}$ black hole, and it is the same level as that seen in the dimmer of the two ASCA observations reported by (Kubota et al. 2005). The radius derived from the DISKBB normalization, $r_{\text{in}}^2 \cos i / (D/10 \text{ kpc})^2 = 26.0 \pm 0.3$ is also consis-

²<http://www.sns.ias.edu/~swd/xspec.html>

TABLE 1
THE BEST FIT PARAMETERS BASED ON THE DISKBB MODEL

model	N_{H} 10^{20} cm^{-2}	T_{in} keV	disk norm ^a	Γ ^b	norm or f ^c	χ^2/dof
diskbb + PL	6.04 ± 0.02	0.840 ± 0.002	26.0 ± 0.3	$2.380^{+0}_{-0.007}$	$0.0354^{+0.0005}_{-0.0006}$	770.25/706
simpl*diskbb	$< 7 \times 10^{-3}$	$0.787^{+0.003}_{-0.001}$	$42.8^{+0.3}_{-0.5}$	$2.380^{+0}_{-0.003}$	$0.115^{+0.0007}_{-0.0023}$	1336.14/706

NOTE.—Errors represent 90 % confidence.

^anormalization is defined as $r_{\text{in}}^2 \cos i / (D/10 \text{ kpc})^2$.

^bValue of photon index Γ is limited to be 2.0–2.38 (see text).

^cPL normalization at 1 keV in the unit of photons $\text{s}^{-1} \text{keV}^{-1}$ or scattering fraction f of the SIMPL model.

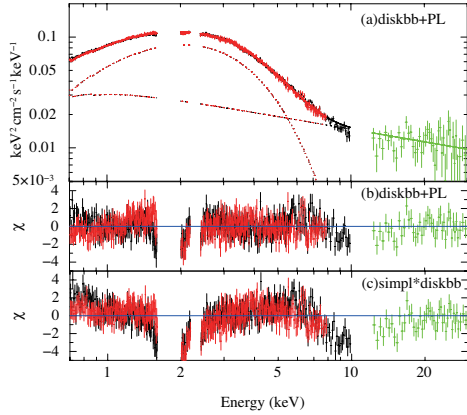


Fig. 2.— νF_{ν} spectrum of LMC X-3 from the best fit DISKBB plus PL model (a), residuals between the data and DISKBB plus PL fit (b) residuals between the data and best fit SIMPL*DISKBB model. In panel (a), the CXB component is subtracted from the PIN spectrum.

tent with the values of 25 ± 3 and 24 ± 2 obtained from the ASCA observations (Kubota et al. 2005).

Even though the fit is good, a closer inspection of the figure shows that this is not a good physical description of a model where the disk provides the seed photons for Compton upscattering into the power law tail as the PL extends below the disk at low energies. Hence we replace the PL model with the SIMPL (Steiner et al. 2008) model for Compton upscattering. This takes some fraction of the disk seed photons and upscatters these to higher energies. It is a convolution model, so requires an extended energy range which we fix at 0.1 keV to 1000 keV.

The fit becomes substantially worse with this more physical model ($\chi^2/dof = 1336/706$), as shown by the residuals between the data and the best fit SIMPL*DISKBB model (Fig. 2c). In addition, N_{H} is much smaller than expected, even though it is comparable to the current systematic uncertainty of the N_{H} determination with the XIS. Both these effects show that the observed disk shape gives the excess at lower energies. In other words, a peak profile of the observed disk spectrum corresponding to the maximum disk temperature is much broader than predicted by DISKBB, motivating us to do more detailed spectral analyses. Similar conclusions were reached by Davis et al. (2006), who analyzed BeppoSAX data. Although their data had poorer signal-to-noise, it had similar low energy coverage and they also found poor fits with DISKBB once the PL was reasonably constrained.

TABLE 2
THE BEST FIT PARAMETERS BASED ON THE KERRBB MODEL

mass M_{\odot}	i degree	N_{H} 10^{20} cm^{-2}	$a^*{}^a$	\dot{M}^b 10^{18} g/s	Γ	f	χ^2/dof
7	67	0.16 ± 0.14	-0.07 ± 0.01	3.32 ± 0.03	$2.38^{+0}_{-0.04}$	$0.093^{+0.002}_{-0.004}$	783.58/706
7	50	0.8 ± 0.1	$0.533^{+0.010}_{-0.007}$	1.27 ± 0.01	$2.37^{+0.01}_{-0.10}$	$0.088^{+0.003}_{-0.008}$	772.86/706
9	67	$0.3^{+0.1}_{-0.1}$	$0.29^{+0.01}_{-0.009}$	2.58 ± 0.02	$2.38^{+0}_{-0.06}$	$0.091^{+0.002}_{-0.005}$	776.33/706
9	50	1.0 ± 0.2	0.738 ± 0.007	1.005 ± 0.009	$2.31^{+0.07}_{-0.09}$	$0.082^{+0.008}_{-0.007}$	776.70/706

NOTE.—Same as table 1 but for the KERRBB model.

^aBlackhole spin parameter.

^bMass accretion rate of the KERRBB model.

3.2. Effect of the general relativity: temperature profile and relativistic smearing : DISKPN and KERRBB

We now use progressively more complex models for the disk emission together with the SIMPL Compton upscattering model for the tail. First, we consider the DISKPN model which includes the stress-free inner boundary condition assuming a Paczynski-Wiita (pseudo-Newtonian) potential. This smoothly connects the temperature profile from $T(r) \propto r^{-3/4}$ at large radii, and $T(r_{\text{in}}) = 0$ at r_{in} , where $r_{\text{in}} = 6R_g$, in a way which is similar to that expected from the fully relativistic equations for a zero spin black hole (Gierliński et al. 1999). This has the effect of broadening the spectrum slightly as it reduces the emission from the hottest material, and hence gives a better fit to the data than the SIMPL*DISKBB ($\chi^2_{\nu} = 984/706$), though still not as good as the unphysical DISKBB+PL model. This indicates that the soft component in the data is still broader than the DISKPN description. Relativistic corrections to the temperature profile alone do not sufficiently broaden the spectrum to match the observed data.

The next step up in complexity is to include the special and general relativistic effects which distort the observed spectrum at each radius. We use the KERRBB model (Li et al. 2005) for this, which calculates the intrinsic temperature distribution from a fully relativistic, stress-free inner boundary condition for arbitrary spin, multiplied by a color temperature correction factor, f_{col} , to approximate the effect of modified blackbody emission. We fixed $f_{\text{col}} = 1.7$ as appropriate for the XIS

CCD bandpass at this luminosity (Done & Davis 2008). This intrinsic emission from each radius is convolved with the relativistic transfer function for that radius and assumed disk inclination (Li et al. 2005).

We explore the dependence on mass and inclination by fitting the model with different combinations of these two parameters. These fit results are shown in table 2 and Fig. 3. These all give a fit which is similarly good as that derived from the DISKBB+PL model (see table 2). The quality of the fit is not very dependent on mass and inclination, but the derived value of the spin changes from almost zero (lowest black hole mass, highest inclination) to ~ 0.7 (highest black hole mass and lowest inclination).

We illustrate the fit in Fig. 3a, showing the νF_{ν} spectrum and residuals for the models with mass of $7M_{\odot}$ and inclination of 67° , as used by Davis et al. (2006). This gives a good fit ($\chi^2_{\nu} = 776/706$) with flat residuals across the whole energy band (see Fig. 3b), and gives a spin of $a^* \simeq 0$, consistent with that derived by Davis et al. (2006). Relativistic effects on the disk continuum were first proposed by Cunningham (1975), but this is the first time they have been significantly detected, as it is much harder to disentangle this smearing on a broad continuum than on a line (Fabian et al. 1989). Though the smaller values of N_{H} may suggest that the data still has excess soft emission and is somewhat broader even than that produced by the temperature profile and relativistic broadening, the calibration uncertainties do not enable us to conclude unambiguously whether there are other broadening factors.

3.3. Effect of the vertical structure of the disk : BHSPEC

The assumption of a constant f_{col} is only an approximation to the true spectrum from a given radius. In the real disk, changes in opacity at atomic edges produce spectra intrinsically broader than a blackbody. Under the assumption of the solar metallicity, the BHSPEC model (Davis et al. 2005) uses radiative transfer to calculate the intrinsic spectrum at a given radius, so does self-consistently include the color temperature correction. It then convolves this with the relativistic transfer functions to produce the best disk spectra to date.

We fit the spectra with the BHSPEC disk model for the same combinations of i and M as for the KerrBB fits above. The results are shown in table 3. The model gives similar spins to those derived from KerrBB (see table 2), showing that the assumption of $f_{\text{col}} = 1.7$ is appropriate to the KerrBB fit for the XIS CCD bandpass. Moreover, the estimated absorption is now consistent with the known column density in this direction $\sim 3 \times 10^{20} \text{ cm}^{-2}$. Thus the BHSPEC model produces additional excess soft emission than produced by relativistic broadening alone. However, despite being a more physical model, it gives a much *worse* fits than KerrBB ($\chi^2/\text{dof} = 1212/706$ for the case of $M = 7M_{\odot}$ and $i = 67^{\circ}$ compared to $783/706$). Figure 4 shows the residuals between the data and the model for each mass and inclination. These are all clearly dominated by a broad feature below 1 keV, which is caused by the smeared atomic absorption edges present in the model.

We checked the result by including relativistically smeared ionised reflection, modelled using the convolution version of the models of Ballantyne et al. (2001) as described in Done & Gierliński (2006). Though the reflection itself cannot be well constrained because of couplings to mass, inclination and the difference of the continuum disk model, it does not change this conclusion: BHSPEC gave a worse fit to the data than KerrBB if we did not constrain its absorption, and the BHSPEC residuals are dominated by features around 1 keV.

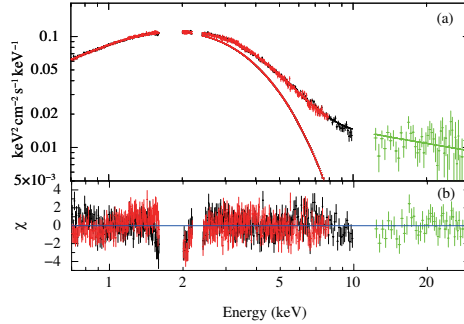


Fig. 3.— νF_{ν} spectrum of LMC X-3 based on the best fit SIMPL*KERRBB model (a), and residuals between the data and the model (b). Same as Fig. 2, the CXB subtracted spectrum is shown for the PIN data (panel a).

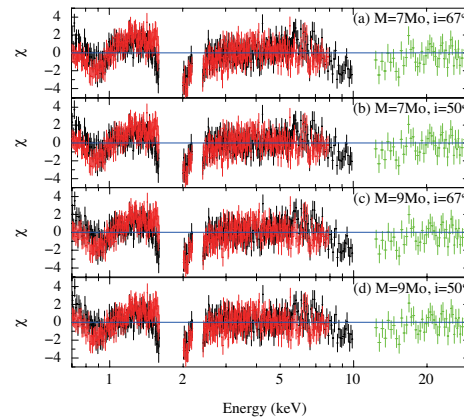


Fig. 4.— Residuals between the data and the best fit BHSPEC models with different mass and inclination. (a) $M = 7M_{\odot}$ and $i = 67^{\circ}$, (b) $M = 7M_{\odot}$ and $i = 50^{\circ}$, (c) $M = 9M_{\odot}$ and $i = 67^{\circ}$, and (d) $M = 9M_{\odot}$ and $i = 50^{\circ}$.

TABLE 3
THE BEST FIT PARAMETERS BASED ON THE BHSPEC MODEL

mass M_{\odot}	i degree	N_{H} 10^{20} cm^{-2}	a^*	L_{disk} 10^{38} erg/s	Γ	f	χ^2/dof
the solar abundance							
7	67	2.7 ± 0.1	$-0.082^{+0.012}_{-0.008}$	1.799 ± 0.005	$2.380^{+0}_{-0.006}$	$0.102^{+0.001}_{-0.002}$	1212.47/706
7	50	3.9 ± 0.1	0.542 ± 0.006	$1.054^{+0.002}_{-0.003}$	$2.380^{+0}_{-0.008}$	0.096 ± 0.002	1058.56/706
9	67	3.1 ± 0.1	0.286 ± 0.009	1.748 ± 0.005	$2.380^{+0}_{-0.006}$	0.100 ± 0.001	1094.30/706
9	50	4.3 ± 0.1	0.742 ± 0.004	$1.085^{+0.002}_{-0.003}$	$2.380^{+0}_{-0.010}$	0.094 ± 0.002	974.65/706
1/3 solar abundance							
7	67	1.6 ± 0.1	-0.076 ± 0.010	$1.765^{+0.005}_{-0.004}$	$2.380^{+0}_{-0.007}$	0.102 ± 0.002	1151.91/706
7	50	2.7 ± 0.1	0.536 ± 0.006	1.033 ± 0.002	$2.380^{+0}_{-0.008}$	0.098 ± 0.002	1062.58/706
9	67	2.0 ± 0.1	0.278 ± 0.009	1.717 ± 0.005	$2.380^{+0}_{-0.006}$	0.102 ± 0.002	1063.26/706
9	50	3.1 ± 0.1	0.737 ± 0.004	1.061 ± 0.002	$2.380^{+0}_{-0.009}$	0.096 ± 0.002	987.75/706
1/10 solar abundance (just for comparison)							
7	67	0.7 ± 0.1	-0.049 ± 0.010	$1.725^{+0.005}_{-0.004}$	$2.380^{+0}_{-0.008}$	0.102 ± 0.002	1014.46/706
7	50	1.69 ± 0.1	$0.552^{+0.007}_{-0.006}$	$1.011^{+0.002}_{-0.003}$	$2.380^{+0}_{-0.008}$	0.099 ± 0.002	974.17/706
9	67	$1.0^{+0.2}_{-0.1}$	$0.304^{+0.009}_{-0.010}$	1.680 ± 0.005	$2.380^{+0}_{-0.009}$	0.101 ± 0.002	973.39/706
9	50	2.0 ± 0.1	0.748 ± 0.004	$1.039^{+0.002}_{-0.003}$	$2.380^{+0}_{-0.010}$	0.097 ± 0.002	919.16/706

NOTE.—Same as table 1 and table 2 but for the BHSPEC model.

3.4. Constraint on the absorption lines due to highly ionized iron

Absorption lines from highly ionized Hydrogen (H-) and Helium(He-) like iron are often seen in disk dominated black hole binaries (see e.g. the compilation in Done et al. 2007). We focus on the iron K line region to sensitively search for such features. We fit the 5-8 keV data with a power law and narrow absorption line (with width fixed at 10 eV). There is evidence for such a line at 6.61 ± 0.04 keV, of equivalent width of -15 ± 6 eV.

Though this is significant at about the 99% confidence level on an F-test as χ^2_{ν} drops from 233/221 to 215/219, the line energy is slightly too low to be He-like iron at 6.70 keV, even if we consider the calibration uncertainty of the gain, ~ 20 eV, when the 1/4 window option is used³. The difference may be even larger, because the lines are often blue shifted due to the disk wind. As seen in the Chandra/HETGS spectra of GX 13+1 (Ueda et al. 2004) and GRS 1915+105 (Ueda et al. 2009), He-like iron energy can be observed at lower energies than the prediction. Ueda et al. (2009) suggested that the slight shift of the line energy can be caused by a possible contamination of less ionized ions such as Li-like ones at 6.68 keV, uncertainties

in the incident line energies for He-like (and more electrons) iron, and/or the velocity-field structure in the wind along the line-of-sight. However, even considering these effects and the XIS calibration uncertainty, 6.61 ± 0.04 keV is still difficult to be interpreted as He-like iron absorption lines. Fixing the line energy at 6.70 keV gives $\chi^2_{\nu} = 226/220$, so again formally significant at the $\sim 99\%$ level, with an equivalent width of -9 ± 6 eV. This value represents the conservative constraint on the He-like iron absorption line.

Other BHB at similar continuum luminosities ($\sim 10^{38} \text{ erg s}^{-1}$) show absorption lines of equivalent width of ~ 30 eV in both H- and He-like iron (e.g., GRO J1655 – 40 (Ueda et al. 1998; Yamaoka et al. 2001; Miller et al. 2006), 1H 1743 – 322 (Miller et al. 2006b)). These BHBs all have similar inclination angle of $i \sim 70^\circ$. Thus less significant absorption lines may indicate that the inclination is likely to be lower than 67° . Alternatively, these BHBs showed higher disk temperature T_{in} than our LMC X-3 data, typically at ≥ 1.0 keV when they showed absorption lines, and thus the disk temperature may also be important in creating the disk wind in addition to the luminosity.

³Based on the CALDB version XIS20090203

4. Discussion & Conclusions

4.1. Black hole spin

The resulting values of spin are fairly similar for both BHSPEC and KERRBB with $f_{\text{col}} = 1.7$, giving a range in spin from 0–0.7 depending on mass and inclination. Although this seems a large range, it only corresponds to a change in inner radius by less than a factor of 2, from $6R_g$ at $a^* = 0$ to $3.4R_g$ at $a^* = 0.7$, whereas for extreme spin at $a^* = 0.998$ the inner radius becomes as small as $1.23R_g$. Thus the models are not very sensitive to spin for low to moderate spin, even for the best constrained black hole system parameters, as the implied change in radius for the last stable orbit is low. However, they are very sensitive to high spin, and strongly rule out such values for LMC X-3.

Hence we conclude that the black hole in LMC X-3 has low-to-moderate spin. This is also the case for all other spin determinations from disk continuum fits (Davis et al. 2006; Shafee et al. 2006; Gou et al. 2009), apart perhaps from GRS 1915 + 105 (McClintock et al. 2006 but see Middleton et al. 2006). Such low to moderate spins are in line with current (but probably quite uncertain) theoretical models which indicate birth spins of $\lesssim 0.8 - 0.9$ from stellar collapse (Gammie et al. 2004). However, we note that the iron line fits often imply rather higher spins, sometime for the same objects (e.g. Miller et al. 2009). This is clearly an area of current intense research, see e.g. the discussion in Kolehmainen & Done (2009).

4.2. Vertical Structure

The Suzaku observation of LMC X-3 shows a spectrum which is dominated by the accretion disk, giving the best data yet on its detailed spectrum, and a simultaneous determination of the high energy tail. We model the tail as Compton upscattering of seed photons from the disk. The disk spectrum is much broader than a simple sum of blackbodies with $T(r) \propto r^{-3/4}$ (DISKBB). It is also broader than a sum of blackbodies with temperature profile given by the (approximate) stress-free inner boundary condition in the pseudo-Newtonian potential (DISKPN). Relativistic smearing of the intrinsic blackbody spectra

from each radius (with temperature profile given by the stress-free inner boundary condition) is required before the model gives a good description of the overall shape of the data (KERRBB), though the KERRBB model also requires an absorption column close to zero.

The BHSPEC model dispenses with the color temperature correction by calculating the spectrum self-consistently from radiative transfer through the vertical structure of the disk. The column density derived from this model is consistent with the known column, but the fit is poor due to residuals at 1 keV. In order to clarify the reason for the residuals seen in the BHSPEC fit, Fig. 5 shows a comparison of the best fit BHSPEC model with that of KERRBB. The BHSPEC model gives more soft emission below 1 keV, and it does this due to the presence of absorption edges, most importantly the K edges of H-like Nitrogen and Oxygen at 0.66 keV and 0.87 keV, respectively. Though these are broadened and smeared by the relativistic effects, they are still deeper than any features present in the data, so appear in the residuals as an excess at the absorption edge energy. These residuals are around 5% (peak to peak), but the data are actually consistent with no structure at these energies, as seen by the featureless residuals from the best fit KERRBB model (Fig. 3b).

To reduce the size of the atomic features, we first consider sub-solar abundances, since the LMC is suggested to have $1/2 \sim 1/3$ solar abundance (Russell & Bessell 1989; Russell & Dopita 1990; Korn et al. 2002). In order to examine this effect, we extended the original BHSPEC model to account for sub-solar metallicity. We fit the data with the new BHSPEC disk model of fixed $1/3$ -solar metallicity for the same combinations of i and M as used previously. The results and fit residuals are shown in table 3 and Fig. 6, respectively. For the condition of $M = 7 M_\odot$ and $i = 67^\circ$, the best fit BHSPEC model with $1/3$ -solar abundance is shown in Fig. 5 together with the original BHSPEC and KERRBB models. The lower abundance means that the absorption edge structure below 1 keV is less significant ($\sim 3\%$ peak-to-peak), which makes the fit slightly better ($\chi^2_\nu = 1152/706$ for $M = 7 M_\odot$ and $i = 67^\circ$), though the residuals are still clearly dominated by the edge structure below 1 keV. We also show the fit results based on the BHSPEC with $1/10$ -solar

abundance in table 3, Fig. 7, and Fig. 5. Even though this is an underestimate of the metallicity, the predicted edge features are still larger than those seen in the data (Fig. 7), and thus the fits are worse than the KERRBB.

This illustrates the key issue. The data indicate that the spectrum is broader than a single color temperature corrected, relativistically smeared model (KERRBB). Including ion opacities as in BHSPEC gives broader spectra, but with the inevitable consequence edge features are predicted. Since there is no evidence for these edges in the spectrum, incorporating sub-solar abundances alone in BHSPEC cannot explain why the model does not reproduce the data.

Instead, this could point to the importance of including more atomic physics in BHSPEC. Currently it only uses bound-free opacity, but bound-bound (line) transitions could also be important, especially if there is large scale turbulence/convective motion in the disk atmosphere. However, if these additional transitions primarily show up as absorption features, they will further enhance the depth of the atomic absorption, increasing the discrepancies. Instead, line and/or radiative recombination continuum emission could fill in some of the absorption features, while still retaining the broader continuum, though this seems somewhat fine-tuned. Self-irradiation of the disk may be a better mechanism, as this would drive the photosphere towards isothermality, removing the atomic features which do not appear to be present in the data but keeping the broader continuum.

Whatever the origin of the fit residuals, their existence demonstrates the possibility of using the observational data to discriminate between different models of the vertical structure of the accretion disk, and motivates development of more sophisticated disk atmosphere calculations.

We are grateful to all the Suzaku team members. The present work is supported by Grant-in-Aid No.19740113 from Ministry of Education, Culture, Sports, Science and Technology of Japan. SWD acknowledges support from the IAS, through grants NSF AST-0807432, NASA NNX08AH24G, and NSF AST-0807444.

REFERENCES

- Ballantyne, D. R., Iwasawa, K., & Fabian, A. C. 2001, *MNRAS*, 323, 506
- Boldt, E. 1987, *Observational Cosmology*, 124, 611
- Gammie, C. F., Shapiro, S. L., & McKinney, J. C. 2004, *ApJ*, 602, 312
- Cowley, A. P., Crampton, D., Hutchings, J. B., Remillard, R., & Penfold, J. E. 1983, *ApJ*, 272, 118
- Cunningham, C. T. 1975, *ApJ*, 202, 788
- Davis, S. W., Blaes, O. M., Hubeny, I., & Turner, N. J. 2005, *ApJ*, 621, 372
- Davis, S. W., Done, C., & Blaes, O. M. 2006, *ApJ*, 647, 525
- Davis, S. W., & Hubeny, I. 2006, *ApJS*, 164, 530
- di Benedetto, G. P. 1997, *ApJ*, 486, 60
- Done, C., & Davis, S. W. 2008, *ApJ*, 683, 389
- Done, C., & Gierliński, M. 2006, *MNRAS*, 367, 659
- Done, C., Gierliński, M., & Kubota, A. 2007, *A&A Rev.*, 15, 1
- Fabian, A. C., Rees, M. J., Stella, L., & White, N. E. 1989, *MNRAS*, 238, 729
- Fukazawa, Y., et al. 2009, *PASJ*, 61, 17
- Gierliński, M., Zdziarski, A. A., Poutanen, J., Coppi, P. S., Ebisawa, K., & Johnson, W. N. 1999, *MNRAS*, 309, 496
- Gou, L., et al. 2009, *ApJ*, 701, 1076
- Kokubun, M., et al. 2007, *PASJ*, 59, 53
- Kolehmainen, M., & Done, C. 2009, *MNRAS* submitted (arXiv:0911.3281)
- Korn, A. J., Keller, S. C., Kaufer, A., Langer, N., Przybilla, N., Stahl, O., & Wolf, B. 2002, *A&A*, 385, 143
- Koyama, K., et al. 2007, *PASJ*, 59, 23
- Kubota, A., Ebisawa, K., Makishima, K., & Nakazawa, K. 2005, *ApJ*, 631, 1062

- Kubota, A., et al. 2007, PASJ, 59, 185
- Li, L.-X., Zimmerman, E. R., Narayan, R., & McClintock, J. E. 2005, ApJS, 157, 335
- Makishima, K., Maejima, Y., Mitsuda, K., Bradt, H. V., Remillard, R. A., Tuohy, I. R., Hoshi, R., & Nakagawa, M. 1986, ApJ, 308, 635
- McClintock, J. E., Shafee, R., Narayan, R., Remillard, R. A., Davis, S. W., & Li, L.-X. 2006, ApJ, 652, 518
- Middleton, M., Done, C., Gierliński, M., & Davis, S. W. 2006, MNRAS, 373, 1004
- Miller, J. M., et al. 2006b, ApJ, 646, 394
- Miller, J. M., Raymond, J., Fabian, A., Steeghs, D., Homan, J., Reynolds, C., van der Klis, M., & Wijnands, R. 2006, Nature, 441, 953
- Miller, J. M., Reynolds, C. S., Fabian, A. C., Miniutti, G., & Gallo, L. C. 2009, ApJ, 697, 900
- Mitsuda, K., et al. 1984, PASJ, 36, 741
- Mitsuda, K., et al. 2007, PASJ, 59, 1
- Negueruela, I., & Coe, M. J. 2002, A&A, 385, 517
- Nowak, M. A., Wilms, J., Heindl, W. A., Pottschmidt, K., Dove, J. B., & Begelman, M. C. 2001, MNRAS, 320, 316
- Novikov, I. D., & Thorne, K. S. 1973, Black Holes (Les Astres Occlus), 343
- Page, M. J., Soria, R., Wu, K., Mason, K. O., Cordova, F. A., & Priedhorsky, W. C. 2003, MNRAS, 345, 639
- Russell, S. C., & Bessell, M. S. 1989, ApJS, 70, 865
- Russell, S. C., & Dopita, M. A. 1990, ApJS, 74, 93
- Serlemitsos, P. J., et al. 2007, PASJ, 59, 9
- Shafee, R., McClintock, J. E., Narayan, R., Davis, S. W., Li, L.-X., & Remillard, R. A. 2006, ApJ, 636, L113
- Shakura, N. I., & Sunyaev, R. A. 1973, A&A, 24, 337
- Shimura, T., & Takahara, F. 1995, ApJ, 445, 780
- Soria, R., Wu, K., Page, M. J., & Sakelliou, I. 2001, A&A, 365, L273
- Steiner, J. F., Narayan, R., McClintock, J. E., & Ebisawa, K. 2008, arXiv:0810.1758
- Takahashi, T., et al. 2007, PASJ, 59, 35
- Ueda, Y., Inoue, H., Tanaka, Y., Ebisawa, K., Nagase, F., Kotani, T., & Gehrels, N. 1998, ApJ, 492, 782
- Ueda, Y., Murakami, H., Yamaoka, K., Dotani, T., & Ebisawa, K. 2004, ApJ, 609, 325
- Ueda, Y., Yamaoka, K., & Remillard, R. 2009, ApJ, 695, 888
- van der Klis, M., Clausen, J. V., Jensen, K., Tjemkes, S., & van Paradijs, J. 1985, A&A, 151, 322
- Yamaoka, K., Ueda, Y., Inoue, H., Nagase, F., Ebisawa, K., Kotani, T., Tanaka, Y., & Zhang, S. N. 2001, PASJ, 53, 179

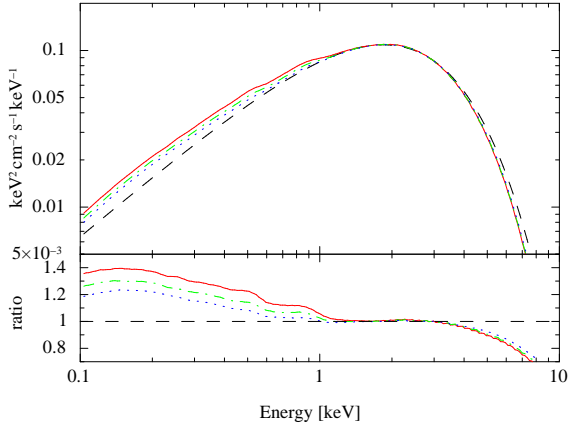


Fig. 5.— Comparison of the best fit BHSPEC and KERRBB (black dashed line) with $i = 67^\circ$ and $M = 7 M_\odot$. The bhspec models are shown with 1-solar abundance (red solid line), 1/3-solar abundance (green dot-dashed line) and 1/10-solar abundance (blue dot line). Ratios of the best fit BHSPEC models to the KERRBB model are shown in the bottom panel. For the plotting purpose, the interstellar absorption and SIMPL are excluded in both models.

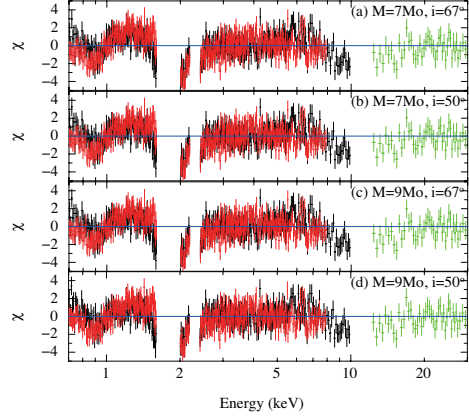


Fig. 6.— Same as Fig. 4 but for 1/3-solar abundance.

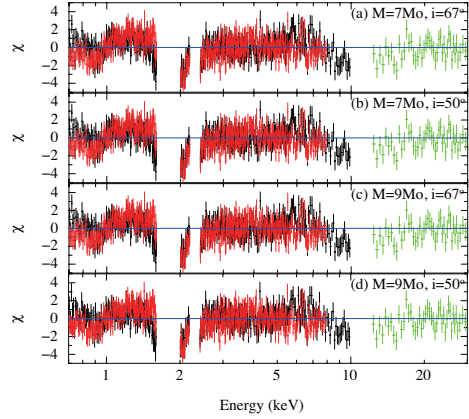


Fig. 7.— Same as Fig. 4 but for 1/10-solar abundance.